

# Helical trajectories of swimming cells with a flexible flagellar hook

Zonghao Zou, Wilson Lough, and Saverio E. Spagnolie\*

Department of Mathematics, University of Wisconsin–Madison,  
480 Lincoln Drive, Madison, Wisconsin 53706, USA

(Dated: April 30, 2022)

The flexibility of the bacterial flagellar hook is believed to have substantial consequences for microorganism locomotion. Using a simplified model of a rigid flagellum and a flexible hook, we show that the paths of axisymmetric cell bodies driven by a single flagellum are generically helical. Phase-averaged resistance and mobility tensors are produced to describe the flagellar hydrodynamics, and a helical rod model which retains a coupling between translation and rotation is identified as a distinguished asymptotic limit. A supercritical Hopf bifurcation in the flagellar orientation beyond a critical ratio of flagellar motor torque to hook bending stiffness, which is set by the spontaneous curvature of the flexible hook, the shape of the cell body, and the flagellum geometry, can have a dramatic effect on the cell’s trajectory through the fluid. Although the equilibrium hook angle can result in a wide variance in the trajectory’s helical pitch, we find a very consistent prediction for the trajectory’s helical amplitude using parameters relevant to swimming *P. aeruginosa* cells.

## I. INTRODUCTION

One of the primary means of prokaryotic microorganism propulsion in viscous fluids is through the rotation of one or many helical flagella, and each flagellum is connected to a rotary motor embedded in the cell membrane by a flexible elastic hook which acts as a joint [1–4]. The bending stiffness of flagellar hooks varies widely, from  $\sim 10^{-4}$  pN  $\mu\text{m}^2$  to  $\sim 10^{-1}$  pN  $\mu\text{m}^2$  [5–10], with smaller values in peritrichous (multi-flagellated) organisms which require the increased flexibility so that the flagella may form flagellar bundles [11]; the hook length itself may be optimized in nature in service to helical bundle stability [12]. The stiffer hook appearing in monotrichous organisms (which propel using a single polar flagellum) appears necessary to stabilize straight swimming, but hook compliance is also needed during the “flick” phase of so-called “run-reverse-flick” trajectories in *V. alginolyticus* during chemotaxis [10, 13]. Although it has been observed in generic settings that a helical flagellum does not substantially *deform* under rotation [14], a more recent investigation by Jabbarzadeh & Fu indicates that both hook as well as flagellum deformability is needed to account for the large hook angles seen in such flicks [15, 16], consistent with experimental observations [13]. Even without the added complexity of a cell body, the chirality of a helical filament results in coupling of translation and rotation which can lead to surprisingly rich dynamics under gravity [17], under magnetic actuation [18, 19], near surfaces [20, 21], in a background flow [22, 23] or even double-helical trajectories for double-helical “superhelices” like insect spermatozoa [24, 25]. For very soft filaments, other instabilities and dynamics abound [26–28].

The end result of such flagellar activity is the body trajectory, itself an object of intense scrutiny. Observations of the helical paths of swimming microorganisms date back as far as the eloquent descriptions by Jennings in 1901 [29]. The helical trajectories of microorganisms have been explored in a very general setting and shown to be demanded by differential geometry under the assumptions of a fixed velocity in the body frame by Crenshaw [30], who used the criterion that a path with fixed curvature and fixed torsion is sufficient to identify a perfect helical trajectory. Helical swimming is a natural consequence when the driving flagellum is tilted at an angle relative to the surface at its connection point to the cell body. In addition to providing a thrust force on the cell, a tilted flagellum, rotated at its base by the rotary motor, will precess in a circular motion relative to the body surface. Though apparently detrimental to motility, this bending angle and precession in fact leads to enhanced mobility in *C. crescentus* [31]. The “wobbling” and “wiggling” of cell bodies has been investigated numerically by Hyon et al., in an effort which included

---

\* spagnolie@math.wisc.edu

comparison to new experiments using *B. subtilis* cells [32], and precession was also noted in simulations by Shum & Gaffney [33]. More recently, Constantino et al. have observed and rationalized the helical trajectories of *H. pylori* [34], Rossi et al. have investigated the same for *E. gracilis* cells [35, 36], synthetic models have been designed to explore helical trajectories [37], and new techniques have been developed for inferring motility parameters statistically [38]. Properly tuned undulatory beating can also result in helical navigation, as found in the swimming of *Chlamydomonas reinhardtii* cells [39].

Parallel to any potential functionality which might be conferred by hook deformability, there are also constraints and requirements on its construction for usability. Vogel & Stark have presented a very detailed picture of flagellum buckling and dynamics, and a supercritical Hopf bifurcation in the thrust force due to hook and flagellum compliance which persists when the flagellum is affixed to a spherical cell body during locomotion [40]. Full numerical simulations and modeling by Shum & Gaffney [33] and Nguyen & Graham [41, 42] confirmed the existence of a critical motor torque triggering a bifurcation from straight swimming to apparently helical swimming trajectories when flagellum flexibility is included (see also Refs. [10, 33, 37]).

In this paper we show using a simplified model of the flagellum and the flagellar hook that a helical trajectory is generic, and study the dependence of the helical path geometry on material parameters including the flagellum geometry, hook bending stiffness, and spontaneous hook curvature. After providing the mathematical description of the swimming cell in §II, we reproduce in §III by very elementary means a modification of the result of Crenshaw [30] that a helical trajectory is generic, through reference to the curvature and torsion observed in a particular reference frame. In §IV we develop the simplified model of a phase-averaged helical flagellum connected by a flexible hook to the cell body which experiences a fixed motor torque. The model is then used to derive analytically the flagellum dynamics when the cell body is fixed in space, and then in the full system in which the cell body, flagellar motion, and hook angle are coupled. We provide analytical expressions for the critical stability criteria, a bifurcation in the hook bending angle which is present in the full swimming problem but not in the fixed-body problem given the assumption of a rigid flagellum. We conclude with a brief discussion in §V.

## II. MATHEMATICAL MODEL

In this paper the cell body is modeled as a prolate spheroid with major and minor axis lengths  $2a$  and  $2b$ , whose position and orientation at time  $t$  evolve according to hydrodynamic force and torque balance. Driving the body through the fluid is a single flagellum connected to the cell by a short, deformable hook. As illustrated in Fig. 1, we define the reference frame (not to be confused with the body frame) to be that in which the centroid of the cell body is located at the origin, and the flagellum orientation, identified by a unit vector  $\mathbf{P}$ , lies in the  $(\mathbf{e}_1, \mathbf{e}_3)$ -plane, with  $\{\mathbf{e}_1, \mathbf{e}_2, \mathbf{e}_3\}$  the standard orthonormal basis. We write  $\mathbf{P} = \sin \phi \mathbf{e}_1 + \cos \phi \mathbf{e}_3$ , and refer to the angle  $\phi$  as the bending angle. The rotary motor which drives the relative rotation between the cell body and flagellar hook is located in the reference frame at position  $\mathbf{X} = a\mathbf{e}_3$ .

In the lab frame, the centroid is located at time  $t$  at a position  $\mathbf{r}(t)$ , and the flagellum orientation is denoted by  $\mathbf{p}(t)$ . The centroid of the cell body evolves as  $\dot{\mathbf{r}} = \mathbf{U}(t)$ , with  $\mathbf{U}$  the translational velocity. The cell's rotational velocity is denoted by  $\boldsymbol{\Omega}$ . As the system translates and rotates it carries with it an orthonormal triad of basis vectors, the columns of the rotation matrix  $\mathbf{D}(t) = \{\mathbf{d}_1(t), \mathbf{d}_2(t), \mathbf{d}_3(t)\}$ , defined such that the position of the flagellar base in the lab frame is given by  $\mathbf{x}(t) = \mathbf{r}(t) + a\mathbf{d}_3(t)$ , and the flagellum direction remains always in the  $(\mathbf{d}_1, \mathbf{d}_3)$ -plane ( $\mathbf{P} \in \text{span}\{\mathbf{e}_1, \mathbf{e}_3\}$  and  $\mathbf{p} \in \text{span}\{\mathbf{d}_1, \mathbf{d}_3\}$ ). The rotational velocity of the flagellum's *orientation* in the lab frame is denoted by  $\boldsymbol{\Omega}^p$ , with  $\boldsymbol{\Omega}^p = \boldsymbol{\Omega} + \dot{\phi}\mathbf{d}_2 + \dot{\theta}\mathbf{d}_3$ , with  $\dot{\theta}$  a flagellar precession rate. Hence the rotational velocity of the orthonormal basis, denoted by  $\boldsymbol{\Omega}_D$ , is given by (with  $\mathbf{d}_3\mathbf{d}_3$  a dyadic product),

$$\boldsymbol{\Omega}_D = (\mathbf{I} - \mathbf{d}_3\mathbf{d}_3) \cdot \boldsymbol{\Omega} + \mathbf{d}_3\mathbf{d}_3 \cdot \boldsymbol{\Omega}^p = \boldsymbol{\Omega} + \dot{\theta}\mathbf{d}_3. \quad (1)$$

With the components of the translational and rotational velocities in the reference frame denoted by  $\mathbf{U}_0$  and  $\boldsymbol{\Omega}_0$ , respectively, we have  $\mathbf{U} = \mathbf{D} \cdot \mathbf{U}_0$  and  $\boldsymbol{\Omega} = \mathbf{D} \cdot \boldsymbol{\Omega}_0$ , and thus  $\boldsymbol{\Omega}_D = \mathbf{D} \cdot (\boldsymbol{\Omega}_0 + \dot{\theta}\mathbf{e}_3)$ . Since the basis vectors (columns

of  $\mathbf{D}$ ) evolve in time via

$$\dot{\mathbf{d}}_i = \boldsymbol{\Omega}_D \times \mathbf{d}_i = (\mathbf{D} \cdot \boldsymbol{\Omega}_0) \times \mathbf{d}_i + \dot{\theta} \mathbf{d}_3 \times \mathbf{d}_i, \quad (2)$$

the rotation matrix evolves according to (using  $\det(\mathbf{D}) = 1$ ),

$$\dot{\mathbf{D}} = \hat{\boldsymbol{\Omega}}_D \cdot \mathbf{D} = (\mathbf{D} \cdot \hat{\boldsymbol{\Omega}}_0 \cdot \mathbf{D}^T + \hat{\boldsymbol{\Omega}}') \cdot \mathbf{D}, \quad (3)$$

where we have introduced the skew-symmetric operators  $\hat{\boldsymbol{\Omega}}_D = \boldsymbol{\Omega}_D \times$ ,  $\hat{\boldsymbol{\Omega}}_0 = \boldsymbol{\Omega}_0 \times$ , and  $\hat{\boldsymbol{\Omega}}' = \dot{\theta} \mathbf{d}_3 \times = \dot{\theta}(\mathbf{d}_2 \mathbf{d}_1 - \mathbf{d}_1 \mathbf{d}_2)$ .

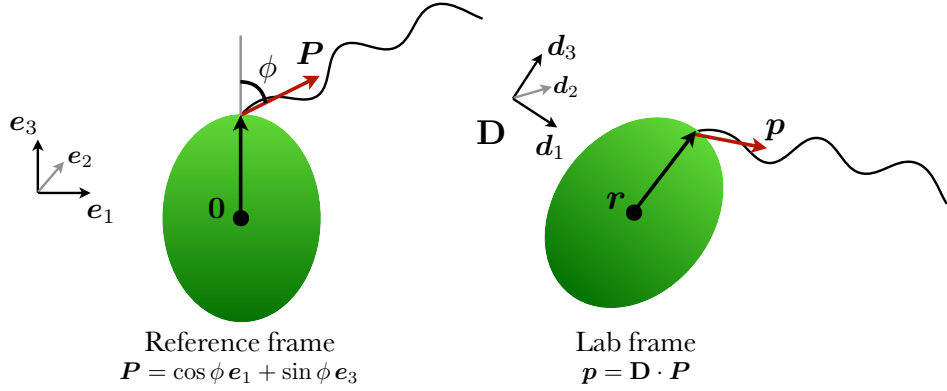


FIG. 1. Schematic of the prolate spheroidal cell body (axis lengths  $2a$  and  $2a\sqrt{1-e^2}$ , with  $e \in [0,1)$  the eccentricity) and flagellum in the reference and lab frames. (Left) Reference frame (not to be confused with the body frame). The flagellum is affixed to a hook emanating from the position  $a\mathbf{e}_3$ , and is oriented in the  $\mathbf{P}(t)$  direction. (Right) Lab frame. The centroid is located at a position  $\mathbf{r}(t)$ , the hook emanates from a position  $\mathbf{x}(t) = \mathbf{r}(t) + a\mathbf{d}_3$ , and the flagellum is oriented in the  $\mathbf{p}(t)$  direction which is always in the  $(\mathbf{d}_1, \mathbf{d}_3)$  plane. Mapping from the reference frame to the lab frame involves a translation by  $\mathbf{r}(t)$  and a rotation via matrix  $\mathbf{D}(t)$ . The bending angle is denoted by  $\phi(t)$ .

For a constant vector  $\mathbf{a}$  and orthonormal  $\mathbf{D}$ , we have that

$$\frac{d}{dt} (\mathbf{D} \cdot \mathbf{a}) = \dot{\mathbf{D}} \cdot \mathbf{a} = (\mathbf{D} \cdot \hat{\boldsymbol{\Omega}}_0 \cdot \mathbf{D}^T + \hat{\boldsymbol{\Omega}}') \cdot (\mathbf{D} \cdot \mathbf{a}) = \mathbf{D} \cdot \left( [\boldsymbol{\Omega}_0 + \dot{\theta} \mathbf{e}_3] \times \mathbf{a} \right). \quad (4)$$

Finally, the flagellum orientation's rotation rate in the body frame is denoted by  $\boldsymbol{\Omega}_0^P$ ; with  $\boldsymbol{\Omega}_0^P = \dot{\phi} \mathbf{e}_2 + \dot{\theta} \mathbf{e}_3$  and  $\boldsymbol{\Omega}^p = \boldsymbol{\Omega} + \mathbf{D} \cdot \boldsymbol{\Omega}_0^P = \mathbf{D} \cdot \left( \boldsymbol{\Omega}_0 + \dot{\theta} \mathbf{e}_3 + \dot{\phi} \mathbf{e}_2 \right)$ , we note that

$$\dot{\mathbf{p}} = \frac{d}{dt} (\mathbf{D} \cdot \mathbf{P}) = \dot{\mathbf{D}} \cdot \mathbf{P} + \mathbf{D} \cdot \dot{\mathbf{P}} = \mathbf{D} \cdot \left[ \left( \boldsymbol{\Omega}_0 + \dot{\theta} \mathbf{e}_3 + \dot{\phi} \mathbf{e}_2 \right) \times \mathbf{P} \right] = \boldsymbol{\Omega}^p \times \mathbf{p}. \quad (5)$$

### III. CONSTANT BENDING ANGLE RESULTS IN A HELICAL TRAJECTORY

We begin by reproducing a modification of the result of Crenshaw [30], that a helical trajectory is almost entirely generic at zero Reynolds number. While Crenshaw shows that a constant translational and rotational velocity in the body frame result in a helical trajectory, here we lean on the axisymmetry of the cell body and produce a similar result by using a reference frame which rotates relative to the flagellar orientation. The primary assumptions that we make are that the flagellum geometry is rigid and that the force and torque generated by the rotation of the flagellum are independent of its phase (thus neglecting small oscillations due to the rotation of a finite helical propeller [43]). It is believed that flagella do not substantially deform during their normal rotating thrust generation [14].

The fully three-dimensional translation and rotation rates of the cell body in the reference frame,  $\mathbf{U}_0(\mathbf{P})$  and  $\boldsymbol{\Omega}_0(\mathbf{P})$ , as well as the evolution of the flagellar orientation in this frame are determined instantaneously in the Stokes flow

limit of zero Reynolds number [44]. Since  $\mathbf{P}$  is described by a single degree of freedom  $\phi \in [0, \pi]$ , and since the system is autonomous by the assumptions above, we must have that  $\phi$  settles to a fixed point (neglecting the special case that the flagellum is in periodically varying hard contact with the cell body). Alternatively, in the frame of the cell body the flagellum orientation vector explores the two-dimensional surface of a sphere, in which case the autonomous system demands that the orientation settles either to a fixed point or a limit cycle. A fixed point is found if either  $\phi = 0$  (or the nonphysical orientation with  $\phi = \pi$ ), or when the relative precession rate between the flagellum and cell body,  $\dot{\theta}$ , is zero. Otherwise, a limit cycle must exist by the Poincaré-Bendixson theorem [45].

We begin by considering the terminal case, in which the flagellum orientation has reached its fixed point in the reference frame (i.e. the bending angle  $\phi$  is constant). By assumption of flagellar phase independence, the cell body velocity and rotation rate in the reference frame,  $\mathbf{U}_0$  and  $\boldsymbol{\Omega}_0$ , are also constant in time, as is the differential precession rate,  $\dot{\theta}$ . We will prove that the resulting trajectory is helical by showing that its curvature,  $\kappa$ , and torsion,  $\tau$ , are constant. In terms of the position of the centroid  $\mathbf{r}(t)$ , and  $\dot{\mathbf{r}} \equiv d\mathbf{r}/dt$ , the curvature and torsion are given by

$$\kappa = \frac{|\dot{\mathbf{r}} \times \ddot{\mathbf{r}}|}{|\dot{\mathbf{r}}|^3}, \quad \tau = \frac{-(\dot{\mathbf{r}} \times \ddot{\mathbf{r}}) \cdot \ddot{\mathbf{r}}}{|\dot{\mathbf{r}} \times \ddot{\mathbf{r}}|^2}. \quad (6)$$

With velocities in the reference frame fixed, we have that

$$\dot{\mathbf{r}} = \mathbf{D} \cdot \mathbf{U}_0, \quad (7)$$

$$\ddot{\mathbf{r}} = \dot{\mathbf{D}} \cdot \mathbf{U}_0 = \mathbf{D} \cdot ([\boldsymbol{\Omega}_0 + \dot{\theta} \mathbf{e}_3] \times \mathbf{U}_0). \quad (8)$$

Upon insertion into (6), we find using manipulations as in (4) and  $|\dot{\mathbf{r}}| = |\mathbf{U}_0|$  that

$$\dot{\mathbf{r}} \times \ddot{\mathbf{r}} = \mathbf{D} \cdot [\mathbf{U}_0 \times ([\boldsymbol{\Omega}_0 + \dot{\theta} \mathbf{e}_3] \times \mathbf{U}_0)], \quad (9)$$

$$\kappa = \frac{|\mathbf{D} \cdot [\mathbf{U}_0 \times ([\boldsymbol{\Omega}_0 + \dot{\theta} \mathbf{e}_3] \times \mathbf{U}_0)]|}{|\mathbf{D} \cdot \mathbf{U}_0|^3} = \frac{|[\mathbf{U}_0 \times ([\boldsymbol{\Omega}_0 + \dot{\theta} \mathbf{e}_3] \times \mathbf{U}_0)]|}{|\mathbf{U}_0|^3}, \quad (10)$$

a constant in time by the assumptions above. The curvature may also be written as

$$\kappa = \frac{\sqrt{AB - Q^2}}{A}, \quad (11)$$

where we have defined

$$A = |\mathbf{U}_0|^2, \quad B = |\boldsymbol{\Omega}_0 + \dot{\theta} \mathbf{e}_3|^2, \quad Q = \mathbf{U}_0 \cdot (\boldsymbol{\Omega}_0 + \dot{\theta} \mathbf{e}_3). \quad (12)$$

Similarly, and again using the identity in (4), we have (again assuming  $\dot{\theta}$  is constant) that

$$\ddot{\mathbf{r}} = \dot{\mathbf{D}} \cdot ([\boldsymbol{\Omega}_0 + \dot{\theta} \mathbf{e}_3] \times \mathbf{U}_0) = \mathbf{D} \cdot ([\boldsymbol{\Omega}_0 + \dot{\theta} \mathbf{e}_3] \times ([\boldsymbol{\Omega}_0 + \dot{\theta} \mathbf{e}_3] \times \mathbf{U}_0)), \quad (13)$$

and therefore

$$\tau = \frac{-\mathbf{D} \cdot [\mathbf{U}_0 \times ([\boldsymbol{\Omega}_0 + \dot{\theta} \mathbf{e}_3] \times \mathbf{U}_0)] \cdot \{\mathbf{D} \cdot ([\boldsymbol{\Omega}_0 + \dot{\theta} \mathbf{e}_3] \times ([\boldsymbol{\Omega}_0 + \dot{\theta} \mathbf{e}_3] \times \mathbf{U}_0))\}}{|\mathbf{D} \cdot [\mathbf{U}_0 \times ([\boldsymbol{\Omega}_0 + \dot{\theta} \mathbf{e}_3] \times \mathbf{U}_0)]|^2} \quad (14)$$

$$= \frac{-[\mathbf{U}_0 \times ([\boldsymbol{\Omega}_0 + \dot{\theta} \mathbf{e}_3] \times \mathbf{U}_0)] \cdot \{[\boldsymbol{\Omega}_0 + \dot{\theta} \mathbf{e}_3] \times ([\boldsymbol{\Omega}_0 + \dot{\theta} \mathbf{e}_3] \times \mathbf{U}_0)\}}{|\mathbf{U}_0 \times ([\boldsymbol{\Omega}_0 + \dot{\theta} \mathbf{e}_3] \times \mathbf{U}_0)|^2} = \frac{-Q}{A}, \quad (15)$$

constant in time. The trajectory is therefore helical with curvature and torsion given by

$$\kappa = \frac{\sqrt{AB - Q^2}}{A}, \quad \tau = \frac{-Q}{A}. \quad (16)$$

The helical trajectory may alternatively be represented by its amplitude,  $\kappa/(\kappa^2 + \tau^2)$ , and its slope  $|\tau|/\kappa$ . The pitch angle is given by  $\tan^{-1}(\kappa/|\tau|)$  (zero for a straight path and  $\pi/2$  for a tightly coiled helical path). The helical amplitude is thus given by  $(AB - Q^2)^{1/2}/B$  and the pitch angle is given by  $\tan^{-1}[\sqrt{AB - Q^2}/Q]$ .

The result above is highly generic. Even if the complete hydrodynamics of the flagellum-cell system are determined exactly, once the (assumed rigid and phase-insensitive) flagellum reaches the fixed point in bending angle the trajectory is assured to be helical, while the flagellum precesses around the normal direction and the cell body translates and rotates, per the calculation above. The terminal flagellum orientation and thus geometry of that helical trajectory may, however, depend on the detailed hydrodynamics of flagellar propulsion. The finite length of real flagella will also contribute very small oscillations due to a small hydrodynamic phase dependence, but the time required for flagellum rotation about its long axis is often small compared to all other timescales in the system, and there may be considerable cancellation of these effects in more general settings.

## IV. TRAJECTORIES OF CELL BODIES WITH A MODEL HELICAL FLAGELLUM

### A. Dynamics of an axisymmetric body

We turn now to the full dynamics of an axisymmetric cell body in a viscous fluid. The linearity of the Stokes equations describing viscous flow demand a linear relationship between the force and torque due to the flagellum and the resultant translational and rotational velocities of the cell body [43]. Although the result of the previous section is generic, we will neglect the hydrodynamic interactions between the cell body and the propelling mechanism for the sake of analytical tractability. Writing the viscous force and torque on the cell body in the reference frame at its centroid as  $\mathbf{F}_0(\mathbf{P})$  and  $\mathbf{M}_0(\mathbf{P})$ , the viscous resistance of a prolate spheroidal cell body results in the translational and rotational velocities in the reference frame,

$$\mathbf{U}_0 = \frac{-1}{6\pi\mu a} [(X^A)^{-1} \mathbf{e}_3 \mathbf{e}_3 + (Y^A)^{-1} (\mathbf{I} - \mathbf{e}_3 \mathbf{e}_3)] \cdot \mathbf{F}_0(\mathbf{P}), \quad (17)$$

$$\mathbf{\Omega}_0 = \frac{-1}{8\pi\mu a^3} [(X^C)^{-1} \mathbf{e}_3 \mathbf{e}_3 + (Y^C)^{-1} (\mathbf{I} - \mathbf{e}_3 \mathbf{e}_3)] \cdot \mathbf{M}_0(\mathbf{P}), \quad (18)$$

where, defining the body eccentricity  $e$  and  $L_e = \ln[(1+e)/(1-e)]$ , we have  $X^A = (8e^3/3)[-2e + (1+e^2)L_e]^{-1}$ ,  $Y^A = (16e^3/3)[2e + (3e^2 - 1)L_e]^{-1}$ ,  $X^C = (4e^3/3)(1-e^2)[2e - (1-e^2)L_e]^{-1}$ , and  $Y^C = (4e^3/3)(2-e^2)[-2e + (1+e^2)L_e]^{-1}$  [46]. If the cell body is spherical,  $e \rightarrow 0$ ,  $X^A = Y^A = X^C = Y^C = 1$ , and

$$\mathbf{U}_0 = \frac{-1}{6\pi\mu a} \mathbf{F}_0(\mathbf{P}), \quad (19)$$

$$\mathbf{\Omega}_0 = \frac{-1}{8\pi\mu a^3} \mathbf{M}_0(\mathbf{P}). \quad (20)$$

To evaluate the swimming path geometry in Eq. (16) we require  $\mathbf{F}_0$  and  $\mathbf{M}_0$  and the flagellum precession rate,  $\dot{\theta}$ , which all require a model of the flagellum, which we develop in the following section. For a concrete example, however, consider a flagellum connected at  $\mathbf{X} = a\mathbf{e}_3$ , oriented in the  $\mathbf{P} = \sin \phi \mathbf{e}_1 + \cos \phi \mathbf{e}_3$  direction, with the bending angle  $\phi$  and precession rate  $\dot{\theta}$  held fixed. If the flagellum is acting on the cell with force  $-f\mathbf{P}$  and moment  $-m\mathbf{P}$ , then

$\mathbf{F}_0 = f\mathbf{P}$  and  $\mathbf{M}_0 = a\mathbf{e}_3 \times \mathbf{F}_0 + m\mathbf{P}$ , and for nearly spherical bodies we find that

$$\kappa = \frac{3}{4a} \left( 1 + \left[ \frac{8\pi\mu a^2 \dot{\theta}}{f} \right]^2 \right)^{1/2} \sin(\phi) + O(e^2), \quad (21)$$

$$\tau = \frac{3}{4a^2 f} (8\pi\mu a^3 \cos(\phi) \dot{\theta} - m) + O(e^2), \quad (22)$$

as  $e \rightarrow 0$ . The trajectory is insensitive to the cell body asphericity to first order in the body eccentricity.

## B. Model flagellum

In this section we will derive the translational and rotational velocities of the cell body, as well as the precession rate,  $\dot{\theta}$ , as functions of the flagellar orientation in the reference frame,  $\mathbf{P}$ . In addition we seek an equation for the time evolution of the bending angle,  $\phi$ . The model of the flagellum will incorporate its geometry and the nontrivial relationship between the motor torque and its dynamics via the flexible hook, to second order in the flagellum amplitude. For this purpose we use the simplest resistive force theory approximation [47, 48] as recently used in similar contexts, including the instability of bodies propelled by  $N$  flagella or swimming with a flexible flagellum near a wall [20, 21, 49], and neglecting hydrodynamic interactions with the cell body. Comparisons between this resistive force theory and full hydrodynamic theory have been explored in detail [48, 50]; a comparison for this precise context in Ref. [42] suggests sufficient accuracy of the simpler resistive force theory for our purposes.

The flagellum is modeled as a slender left-handed helical filament of length  $L$  and amplitude  $b$ , with aspect ratio (diameter/length, “slenderness”) denoted by  $\varepsilon$ , with  $0 < \varepsilon \ll 1$ . We parameterize the flagellum by arc-length  $s \in [0, L]$ , describing the position on the flagellum at station  $s$  and time  $t$  in the reference frame by  $\mathbf{X}^f(s, t) = \mathbf{X} + \alpha s \mathbf{P}(t) + b(\cos(ks - \delta) \mathbf{P}^\perp(t) - \sin(ks - \delta) \mathbf{P}^{\perp\perp}(t))$ , with  $\{\mathbf{P}, \mathbf{P}^\perp, \mathbf{P}^{\perp\perp}\}$  an orthonormal basis. The position  $\mathbf{X} = a\mathbf{e}_3$  denotes the constant location in the reference frame of the rotary motor connecting the cell body to the flagellar hook. We set  $\alpha = \sqrt{1 - (kb)^2}$  so that the parameter  $s$  is the arc-length, and  $\delta$  is a phase constant. The tapering of the helical radius needed to bridge the hook to the flagellum is neglected for convenience; the inclusion of tapering has been found elsewhere to play a minimal role in this context [33]. Assuming the flagellum to be rigid with translation velocity  $\mathbf{U}_0^f$  and rotation rate  $\boldsymbol{\Omega}_0^f$  in the reference frame, the filament velocity (and thus fluid velocity, by the assumption of a no-slip boundary condition) at station  $s$  along the filament is given in the reference frame by  $\mathbf{u}_0(s) = \mathbf{U}_0^f + \boldsymbol{\Omega}_0^f \times (\mathbf{X}^f(s, t) - \mathbf{X})$ .

To relate back to §II and Fig. 1, the rotational velocity of the flagellum in the *body* frame,  $\boldsymbol{\Omega}_0^f - \boldsymbol{\Omega}_0$ , is composed of the rotation rate of its orientation vector  $\mathbf{P}$  along with an additional (unknown) spin rate  $\omega$  about  $\mathbf{P}$ , and we write  $\boldsymbol{\Omega}_0^f - \boldsymbol{\Omega}_0 = \omega \mathbf{P} + \boldsymbol{\Omega}_0^P = \omega \mathbf{P} + \dot{\phi} \mathbf{e}_2 + \dot{\theta} \mathbf{e}_3$ . The rate of change of the bending angle, the precession rate, and the spin rate are then computed as

$$\dot{\phi} = \mathbf{e}_2 \cdot (\boldsymbol{\Omega}_0^f - \boldsymbol{\Omega}_0), \quad (23)$$

$$\dot{\theta} = (\mathbf{e}_3 - \cot(\phi) \mathbf{e}_1) \cdot (\boldsymbol{\Omega}_0^f - \boldsymbol{\Omega}_0), \quad (24)$$

$$\omega = \csc(\phi) \mathbf{e}_1 \cdot (\boldsymbol{\Omega}_0^f - \boldsymbol{\Omega}_0). \quad (25)$$

The reference frame viscous drag per unit length on the flagellum,  $\mathbf{f}_0$ , we model using resistive force theory,

$$\mathbf{f}_0(s) = -\frac{8\pi\mu}{c+2} \left[ \mathbf{I} + \frac{2-c}{2c} \hat{\mathbf{s}} \hat{\mathbf{s}} \right] \cdot \mathbf{u}_0(s), \quad (26)$$

where  $c = \log(1/\varepsilon^2) - 1$  ( $> 0$ ), and  $\hat{\mathbf{s}} = \partial_s \mathbf{X}^f(s)$  is the unit tangent vector. The total viscous force and torque on the flagellum measured relative to  $\mathbf{X}$ , denoted by  $\mathbf{F}_0^f$  and  $\mathbf{M}_0^f$ , respectively, are determined by integration over the

filament length,

$$\mathbf{F}_0^f = \int_0^L \mathbf{f}_0(s) ds, \quad (27)$$

$$\mathbf{M}_0^f = \int_0^L (\mathbf{X}^f(s) - \mathbf{X}) \times \mathbf{f}_0(s) ds. \quad (28)$$

Averaging over the phase,  $\delta$ , and inserting  $\mathbf{f}$  from above, we have the general linear resistance relations

$$\mathbf{F}_0^f = -\mathbf{A} \cdot \mathbf{U}_0^f - \mathbf{B} \cdot \mathbf{\Omega}_0^f, \quad (29)$$

$$\mathbf{M}_0^f = -\mathbf{B}^T \cdot \mathbf{U}_0^f - \mathbf{D} \cdot \mathbf{\Omega}_0^f, \quad (30)$$

(see Ref. [43]) where the individual block operators are simplified using (phase-averaged) axisymmetry,

$$\mathbf{A} = \left( \frac{2\pi\mu L}{c} \right) (\xi_1 \mathbf{P} \mathbf{P} + \xi_2 (\mathbf{I} - \mathbf{P} \mathbf{P})), \quad (31)$$

$$\mathbf{B} = \left( \frac{2\pi\mu L^2}{c} \right) (\eta_1 \mathbf{P} \mathbf{P} + \eta_2 (\mathbf{I} - \mathbf{P} \mathbf{P}) + \eta_3 (\mathbf{P}^\perp \mathbf{P}^{\perp\perp} - \mathbf{P}^{\perp\perp} \mathbf{P}^\perp)), \quad (32)$$

$$\mathbf{D} = \left( \frac{2\pi\mu L^3}{c} \right) (\zeta_1 \mathbf{P} \mathbf{P} + \zeta_2 (\mathbf{I} - \mathbf{P} \mathbf{P})). \quad (33)$$

Keeping terms up to  $O(b^4 k^4)$  in a small-amplitude approximation of the flagellum, we compute the dimensionless quantities

$$\xi_1 = 2(1 + b^2 k^2), \quad \xi_2 = 4 - b^2 k^2, \quad (34)$$

$$\eta_1 = 2b^2 k/L, \quad \eta_2 = -b^2 k/L, \quad \eta_3 = 2 - 3b^2 k^2/2, \quad (35)$$

$$\zeta_1 = 4b^2/L^2, \quad \zeta_2 = \frac{1}{3} (4 - 5b^2 k^2 + 3b^2/L^2). \quad (36)$$

The off-diagonal tensor may be made symmetric by a parallel translation to the center of hydrodynamic reaction, but since we will match forces and torques at an endpoint we leave the structure above.

Inverting the resistance equations (29)-(30), we find the mobility relations,

$$\mathbf{U}_0^f = -\tilde{\mathbf{A}} \cdot \mathbf{F}_0^f - \tilde{\mathbf{B}} \cdot \mathbf{M}_0^f, \quad (37)$$

$$\mathbf{\Omega}_0^f = -\tilde{\mathbf{B}}^T \cdot \mathbf{F}_0^f - \tilde{\mathbf{D}} \cdot \mathbf{M}_0^f, \quad (38)$$

where the individual block operators are given by

$$\tilde{\mathbf{A}} = \left( \frac{c}{8\pi\mu L} \right) (\alpha_1 \mathbf{P} \mathbf{P} + \alpha_2 (\mathbf{I} - \mathbf{P} \mathbf{P})), \quad (39)$$

$$\tilde{\mathbf{B}} = \left( \frac{c}{8\pi\mu L^2} \right) (\beta_1 \mathbf{P} \mathbf{P} + \beta_2 (\mathbf{I} - \mathbf{P} \mathbf{P}) + \beta_3 (\mathbf{P}^\perp \mathbf{P}^{\perp\perp} - \mathbf{P}^{\perp\perp} \mathbf{P}^\perp)), \quad (40)$$

$$\tilde{\mathbf{D}} = \left( \frac{c}{8\pi\mu L^3} \right) (\gamma_1 \mathbf{P} \mathbf{P} + \gamma_2 (\mathbf{I} - \mathbf{P} \mathbf{P})), \quad (41)$$

with the dimensionless quantities

$$\alpha_1 = 2 - b^2 k^2, \quad \alpha_2 = 4 + b^2 k^2 - 9b^2/L^2, \quad (42)$$

$$\beta_1 = -kL (1 - b^2 k^2/2), \quad \beta_2 = 3b^2 k/L, \quad \beta_3 = -\frac{3}{2} (4 + 3b^2 k^2 - 12b^2/L^2), \quad (43)$$

$$\gamma_1 = \frac{L^2}{4b^2} (4 + 2b^2 k^2 - b^4 k^4), \quad \gamma_2 = 3 (4 + 5b^2 k^2 - 12b^2/L^2). \quad (44)$$

The viscous force and torque on the flagellum,  $\mathbf{F}_0^f$  and  $\mathbf{M}_0^f$ , depend on the interaction with the cell body as mediated by the flexible hook. In the following sections we consider the cases of: prescribed forces and moments acting on the flagellum; a flexible connection to a stationary cell body; and a flexible connection to a freely moving cell body.

### C. No cell body, prescribed forces and moments

As a simple example, if the flagellum is subject to a force  $f\mathbf{P}$  and a moment  $m\mathbf{P}$  applied at the basal connection point,  $\mathbf{X}$ , the viscous force and torque on the flagellum about the basal connection point are  $\mathbf{F}_0^f = -f\mathbf{P}$  and  $\mathbf{M}_0^f = -m\mathbf{P}$ , and the resulting velocity and rotation rate about  $\mathbf{X}$  are given by  $\mathbf{U}_0^f = U_f\mathbf{P}$  and  $\mathbf{\Omega}_0^f = \Omega_f\mathbf{P}$ , where

$$U^f = \frac{c}{8\pi\mu L} (2 - b^2 k^2) \left( f - \frac{k}{2} m \right) + O(b^4 k^4), \quad (45)$$

$$\Omega^f = \frac{ck}{16\pi\mu L} \left( - (2 - b^2 k^2) f + k \left( \frac{2}{b^2 k^2} + 1 - \frac{b^2 k^2}{2} \right) m \right) + O(b^4 k^4). \quad (46)$$

If  $f = 0$  and  $m > 0$  then the left-handed helix rotates about the  $\mathbf{P}$  axis ( $\Omega^f > 0$ ), with waves appearing to pass in the direction away from the cell and generating a force on the fluid in the  $\mathbf{P}$  direction; the fluid reaction pushes the cell in the  $-\mathbf{P}$  direction ( $U^f < 0$ ). These directions are flipped for a right-handed helix ( $k \rightarrow -k$ ).

A subtle point arises in the limit that  $b \rightarrow 0$ , in which the helix tends towards the shape of a straight rod. Since we have neglected the rotational drag around the long axis of the filament locally, which scales as  $O(\varepsilon^2)$  as  $\varepsilon \rightarrow 0$ , the rotation rate above tends towards infinity as  $b \rightarrow 0$ . Nevertheless the coupling between the torque and the translational speed of such a filament does not vanish in this limit, instead it tends towards dependence on the wavenumber,  $k$ . A more detailed examination of this asymptotic regime shows that the model above amounts to a distinguished limit, accurate so long as  $\varepsilon L/b$  is held fixed as  $b \rightarrow 0$  [51]. At leading order in  $c$ , the tensors above remain accurate; contributions which depend on the fixed value of  $\varepsilon L/b$  enter at  $O(1)$ . We refer the reader also to the related model by Vogel & Stark in Ref. [40], there named the ‘helical rod model’, which in addition to hydrodynamics incorporates filament deformability and bending stiffness.

### D. Model hook, and a fixed cell body

The relationship between the viscous force and torque on the cell body and those on the flagellum are mediated by a small flexible hook, which we model using a discretization of the Kirchhoff elastic rod theory with only a single joint. The effective (integrated) curvature is related to the bending angle  $\phi$  with the elastic energy stored in the hook (i.e. in the joint connecting the cell body to the flagellum); penalizing deviations of the curvature away from a preferred angle,  $\phi_0$ , we write  $\mathcal{E}_b = (2B/\ell_h) (\tan(\phi/2) - \tan(\phi_0/2))^2$ , where  $B$  is the bending stiffness (with units of energy times length) and  $\ell_h$  is the length of the hook [52, 53]. This energy penalty results in the Bernoulli-Euler elastic moment internal to the hook in the lab frame given by  $(2B/\ell_h) (\tan(\phi/2) - \tan(\phi_0/2)) \mathbf{d}_2$ . Experimental measurements report  $\ell_h \sim 50 - 100\text{nm}$ , which is much smaller than standard flagellum lengths  $L \sim 1 - 10\mu\text{m}$  [5–7, 10, 54–57].

The base of the hook is assumed to be oriented normal to the surface at its connection point to the cell body. The short hook (and thus flagellum) is driven at its base with a constant motor torque  $M_a \mathbf{e}_3$ , with  $M_a$  assumed known. This moment must be balanced by a viscous torque on the cell body, or  $\mathbf{e}_3 \cdot \mathbf{M}_0 = M_a$ . More detailed continuous Kirchhoff rod models have been used in related numerical studies [15, 40, 41, 58]; see also Ref. [53].

With the hook assumed to be very short compared to other length scales in the problem, we arrive at the following

system of equations:

$$\mathbf{F}_0 + \mathbf{F}_0^f = \mathbf{0}, \quad (47)$$

$$\mathbf{M}_0 + a\mathbf{e}_3 \times \mathbf{F}_0^f + \mathbf{M}_0^f = \mathbf{0}, \quad (48)$$

$$\mathbf{M}_0^f - 2B(\tan(\phi/2) - \tan(\phi_0/2))\mathbf{e}_2 + M_a\mathbf{e}_3 = \mathbf{0}, \quad (49)$$

$$\mathbf{U}_0^f = \mathbf{U}_0 + a\boldsymbol{\Omega}_0 \times \mathbf{e}_3, \quad (50)$$

where  $\mathbf{U}_0$  and  $\boldsymbol{\Omega}_0$  are related to  $\mathbf{F}_0$  and  $\mathbf{M}_0$  via (17)-(18),  $\mathbf{U}_0^f$  and  $\boldsymbol{\Omega}_0^f$  are related to  $\mathbf{F}_0^f$  and  $\mathbf{M}_0^f$  via (37)-(38). These equations represent, in order: total force balance, total torque balance about the cell body centroid, torque balance on the flagellum about the basal connection point, and the kinematic constraint of flagellum attachment to the cell body. The unknowns depend on the problem of interest.

Consider first the case that the cell body position and orientation are pinned in space in the reference frame,  $\mathbf{U}_0 = \mathbf{0}$  and  $\boldsymbol{\Omega}_0 = \mathbf{0}$  (and hence  $\mathbf{U}_0^f = \mathbf{0}$ ), by an external body force  $\mathbf{F}_{ext} = \mathbf{F}_0$  and torque  $\mathbf{M}_{ext} = \mathbf{M}_0$  which now act as Lagrange multipliers. Equations (47)-(50) then reduce to three vector equations which are solved for the variables  $\{\mathbf{F}_0, \mathbf{M}_0, \boldsymbol{\Omega}_0^f\}$ , resulting in the following angular velocity of the flagellum:

$$\boldsymbol{\Omega}_0^f = \frac{cM_a}{8\pi\mu L^3} \left[ \frac{L^2}{b^2} \cos(\phi) \mathbf{P} - \eta \sin(\phi) \mathbf{P}^\perp \right] - \frac{cB\eta}{4\pi\mu L^3 \ell_h} (\tan(\phi/2) - \tan(\phi_0/2)) \mathbf{P}^{\perp\perp}, \quad (51)$$

with  $\mathbf{P}^\perp = \cos(\phi)\mathbf{e}_1 - \sin(\phi)\mathbf{e}_3$ ,  $\mathbf{P}^{\perp\perp} = \mathbf{e}_2$ , and

$$\eta = \gamma_2 - \frac{\beta_2^2 + \beta_3^2}{\alpha_2} = 3 + \frac{3b^2 k^2}{4} \left( 5 - \frac{3}{k^2 L^2} \right) + O(k^4 b^4). \quad (52)$$

The rotational velocity may instead be decomposed into its bending, precession and spin (with errors on the scale of  $O(b^4 k^4)$ ) as

$$\dot{\phi} = -\frac{cB\eta}{4\pi\mu L \ell_h} \left( \tan\left(\frac{\phi}{2}\right) - \tan\left(\frac{\phi_0}{2}\right) \right), \quad \dot{\theta} = \frac{c\eta M_a}{8\pi\mu L^3}, \quad \omega = \frac{1}{8\pi\mu L b^2} - \frac{\eta}{8\pi\mu L^3}. \quad (53)$$

The precession rate is perhaps surprisingly independent of the bending angle, but the same viscous moment resists the lateral flagellum motion regardless of bending orientation. The force and moment required to maintain a motionless cell body do, however, depend on the bending angle.

With the body fixed in space the bending component is decoupled from the rest of the rotation, evolving until it reaches a fixed point, in this case the preferred hook angle  $\phi_0$ . This equilibrium hook angle is stable, per observation of Eq. (51). Upon equilibration, with  $\phi = \phi_0$  the external force and torque required to pin the cell body are, with  $\mathbf{P}^\perp = \cos(\phi)\mathbf{e}_1 - \sin(\phi)\mathbf{e}_3$  and  $\mathbf{P}^{\perp\perp} = \mathbf{e}_2$ ,

$$\mathbf{F}_{ext} = \frac{M_a}{L} \left\{ \frac{-\beta_1}{\alpha_1} \cos(\phi_0) \mathbf{P} + \frac{\beta_2}{\alpha_2} \sin(\phi_0) \mathbf{P}^\perp - \frac{\beta_3}{\alpha_2} \sin(\phi_0) \mathbf{P}^{\perp\perp} \right\}, \quad (54)$$

and

$$\mathbf{M}_{ext} = M_a \left\{ \left( \cos(\phi_0) + \frac{a\beta_3}{L\alpha_2} \sin^2(\phi_0) \right) \mathbf{P} - \sin(\phi_0) \left( 1 - \frac{a\beta_3}{L\alpha_2} \cos(\phi_0) \right) \mathbf{P}^\perp - \frac{a}{2L\alpha_1\alpha_2} \sin(2\phi_0) (\alpha_2\beta_1 - \alpha_1\beta_2) \mathbf{P}^{\perp\perp} \right\}. \quad (55)$$

One might expect the force required to increase with the length of the flagellum, but that assumes fixed flagellar rotation rate; with the motor torque fixed the rotation rate diminishes as  $1/L$ , and the resulting force is thus independent

of  $L$  (to leading order in the helical amplitude). Upon phase averaging over a full precession cycle, we find

$$\langle \mathbf{F}_{ext} \rangle = \frac{kM_a}{2} \left( \cos^2(\phi_0) - \frac{3b^2}{2L^2} \sin^2(\phi_0) \right) \mathbf{e}_3 + O(b^4 k^4), \quad (56)$$

and  $\langle \mathbf{M}_{ext} \rangle = M_a \mathbf{e}_3$ , with the  $b \rightarrow 0$  limit again remaining informative. With positive motor torque  $M_a$  the left-handed helix is viewed as passing waves up away from the body, pushing the cell body downward and requiring an external force in the positive  $\mathbf{e}_3$  direction to maintain the cell's position. Note that Vogel & Stark in Ref. [40] show the onset of a flagellum bending instability in the pinned case beyond a critical motor torque, a self-driven Euler-buckling similarities to that found in sedimenting [59] and axially-driven rods [60] (see Ref. [61] for a general overview).

### E. The cell body moves

Finally, we consider the full picture in which the cell body motion and flagellum motion are coupled. This amounts to the solution of the four vector equations (47)-(50) for the variables  $\{\mathbf{U}_0, \boldsymbol{\Omega}_0, \mathbf{U}_0^f, \boldsymbol{\Omega}_0^f\}$ . The simplest case is the axisymmetric configuration in which the preferred flagellar orientation is normal to the cell body, or  $\phi_0 = 0$ , and the bending angle is zero,  $\phi = 0$ . Then  $\dot{\phi} = 0$ , and extracting the precession and spin rates from Eqs. (23)-(25) we obtain the translation and rotation rates

$$\mathbf{U}_0 = \frac{\beta_1 M_a}{2\pi\mu L(3a\alpha_1 X^A + 4Lc^{-1})} \mathbf{e}_3 = \frac{-ckM_a}{4\pi\mu(3acX^A + 2L)} \left( 1 - \frac{b^2 k^2 L}{3acX^A + 2L} \right) \mathbf{e}_3 + O(b^2 k^2), \quad (57)$$

$$\boldsymbol{\Omega}_0 = -\frac{M_a}{8\pi a^3 \mu X^C} \mathbf{e}_3, \quad (58)$$

which are constant in time, as the body swims along in a straight path. Generally, however, for preferred bending angle  $\phi_0$  and instantaneous bending angle  $\phi$ , the body translation and rotation rates depend on the complete body and flagellum geometries (see Appendix A). But writing  $\dot{\phi} = \mathbf{e}_2 \cdot (\boldsymbol{\Omega}_0^f - \boldsymbol{\Omega}_0)$  they reveal an equation describing the dynamics of the bending angle alone (even while the entire system translates and rotates and the flagellum precesses):

$$\dot{\phi} = -\frac{B}{8\pi\mu L^3 \ell_h} \left( \left[ \tan\left(\frac{\phi}{2}\right) - \tan\left(\frac{\phi_0}{2}\right) \right] C_1(\phi) - \tilde{M}_a \lambda \sin(\phi) C_2(\phi) \right), \quad (59)$$

where  $\tilde{M}_a = M_a/(B/\ell_h)$  is a dimensionless active moment and  $\lambda = L/a$  is the scaled flagellum length, and the functions  $C_1(\phi)$  and  $C_2(\phi)$  are given in Appendix A. In the slender flagellum limit, however, we have

$$C_1(\phi) = 2c\eta + \frac{1}{Y^C} [2\lambda^3 + 5\lambda^2 m_3 \cos(\phi) + 3m_3^2 \lambda Y^C (Q_2 + Q_1 \cos(2\phi))] + O(\lambda/c), \quad (60)$$

$$C_2(\phi) = \frac{\lambda m_2}{Y^C} \cos(\phi) + Q_1 m_3 (m_1 + m_2 \cos(2\phi)) + O(\lambda/c), \quad (61)$$

as  $c/\lambda \rightarrow \infty$ , where  $\eta$  is given in Eq. (52) and we have defined

$$m_1 = -\left(\frac{\beta_1}{\alpha_1} + \frac{\beta_2}{\alpha_2}\right) = \frac{kL}{2} \left( 1 - \frac{3b^2}{2L^2} \right) + O(b^4 k^4), \quad (62)$$

$$m_2 = -\left(\frac{\beta_1}{\alpha_1} - \frac{\beta_2}{\alpha_2}\right) = \frac{kL}{2} \left( 1 + \frac{3b^2}{2L^2} \right) + O(b^4 k^4), \quad (63)$$

$$m_3 = -\frac{2\beta_3}{3\alpha_2} = 1 + \frac{1}{2} b^2 k^2 \left( 1 - \frac{3}{2(kL)^2} \right) + O(b^4 k^4), \quad (64)$$

$$Q_1 = \frac{3}{4Y^C} + \frac{1}{Y^A} - \frac{1}{X^A}, \quad Q_2 = \frac{1}{X^A} + \left( 1 + 2 \left( \frac{\beta_2}{\beta_3} \right)^2 \right) \left( \frac{1}{Y^A} + \frac{3}{4Y^C} \right). \quad (65)$$

In the limit of a very large cell body or very short flagellum,  $\lambda \rightarrow 0$ , the problem reduces to that studied in the previous section: the base of the flagellum is effectively pinned on a wall;  $C_1(\phi; \phi_0) = 2c\eta Y^C$  and  $C_2(\phi) = 0$ , and  $\phi$  rapidly relaxes to its preferred value of  $\phi_0$ .

Substantial simplification ensues when considering nearly spherical bodies and small flagellar helical amplitudes, leaving simply

$$C_1(\phi) = \frac{1}{\nu(\phi)} \left( 6c + \frac{2\lambda^2}{3c} (3\lambda^2 + 6\lambda \cos(\phi) + 14) + \frac{\lambda}{2} (4\lambda^2 + 12\lambda \cos(\phi) + 3(11 + \cos(2\phi))) + \frac{4\lambda^5}{9c^2} \right) + O(b^2 k^2, e^2), \quad (66)$$

$$C_2(\phi) = \frac{kL \cos(\phi)}{12\nu(\phi)} (6\lambda + 9 \cos(\phi) + 2c^{-1}\lambda^2) + O(b^2 k^2, e^2), \quad (67)$$

with  $\nu(\phi) = 1 + c^{-1}\lambda(11 - \cos(2\phi))/8 + 7c^{-2}\lambda^2/18 + O(b^2 k^2, e^2)$ , as  $bk \rightarrow 0$  and  $e \rightarrow 0$ .

### 1. Straight swimming is unstable beyond a critical active moment

Is the straight swimming configuration, with  $\phi_0 = 0$  and  $\phi = 0$ , stable? Expanding Eq. (59) about small  $\phi$  (without assuming  $\lambda/c$  to be small), we find the linearized equation

$$\dot{\phi} = -\frac{B}{8\pi\mu L^3 \ell_h} \left( \frac{1}{2} \tilde{C}_1 - \lambda \tilde{M}_a \tilde{C}_2 \right) \phi, \quad (68)$$

with

$$\tilde{C}_1 = \frac{1}{3\alpha_2 + \lambda c^{-1} Q_3} \left( 6c\alpha_2\eta + 2\lambda\gamma_2 Q_3 + \frac{6}{Y^C} (-2\beta_3\lambda^2 + \alpha_2\lambda^3) + \frac{8\lambda^4}{cY^A Y^C} \right), \quad (69)$$

$$\tilde{C}_2 = \frac{1}{(\alpha_1 X^A + 4\lambda(3c)^{-1})(3\alpha_2 + \lambda c^{-1} Q_3)} \left( 4X^A Q_1 \beta_1 \beta_3 + \frac{3\lambda X^A}{Y^C} \alpha_1 \alpha_2 m_2 + \frac{4\lambda^2(\beta_2 - \beta_1)}{cY^C} \right). \quad (70)$$

and  $Q_3 = 3/Y^C + 4/Y^A$ . A critical orientational instability is thus observed when the active dimensionless motor torque  $\tilde{M}_a = M_a/(B/\ell_h)$  crosses a threshold  $\tilde{M}_a^* := \tilde{C}_1/(2\lambda\tilde{C}_2)$ , or

$$\tilde{M}_a^* = \frac{(\alpha_1 X^A + 4\lambda(3c)^{-1}) (6c\alpha_2\eta + 2\lambda\gamma_2 Q_3 + (2/Y^C) (-6\beta_3\lambda^2 + 3\alpha_2\lambda^3 + 4c^{-1}\lambda^4/Y^A))}{4X^A Q_1 \beta_1 \beta_3 + 3\lambda X^A \alpha_1 \alpha_2 m_2 / Y^C + 4c^{-1}\lambda^2(\beta_2 - \beta_1) / Y^C}. \quad (71)$$

In the small helical amplitude limit  $bk \rightarrow 0$ , this may be written as

$$\tilde{M}_a^* = \frac{c}{ak\lambda^2} \mathcal{F}(\lambda, e, c) + O(b^2 k^2), \quad (72)$$

where

$$\mathcal{F}(\lambda, e, c) = \frac{4 (3X^A + 2\lambda c^{-1}) (9Y^A Y^C + 3\lambda c^{-1} ((\lambda^2 + 3\lambda + 3) Y^A + 4Y^C) + \lambda^4 c^{-2})}{9[(3 + 2\lambda)X^A Y^A + 4X^A Y^C - 4Y^A Y^C] + 6\lambda^2 Y^A c^{-1}}. \quad (73)$$

Figure 2 shows the contours of  $\mathcal{F}$  for  $c = 10$  and  $c = 100$  across a range of flagellum lengths,  $\lambda = L/a$ , and body eccentricities,  $e$ . When the flagellum is substantially aspherical ( $e$  increasing towards 1), straight swimming tends to be less stable in the sense that the critical active moment before instability is reduced. As shown in the leftmost panel with  $c = 10$ , the critical active motor torque is generically non-monotonic in the flagellum length, as described by Nguyen & Graham [41]. As  $\lambda \rightarrow 0$ ,  $\tilde{M}_a^* \sim (3c)/(akQ_1\lambda^2)$ , a singularity indicating that the active motor torque required to destabilize the system grows without bound as the relative flagellum length goes to zero (or the cell body size becomes large). This is consistent with the limiting case of a fixed body studied in the previous section.

Meanwhile, for large  $\lambda$ ,  $\tilde{M}^* \sim 4\lambda/(3ackY^A)$  as  $\lambda \rightarrow \infty$ , and once again in this limit the motor torque required to destabilize the system becomes very large. Note that the non-monotonicity of the critical active moment  $\tilde{M}_a^*$  is not observed if terms of order  $c/\lambda$  are not retained. For yet a clearer inspection, assuming a spherical cell body,  $e = 0$ , we find

$$\tilde{M}_a^* = \left( \frac{4(3c + 2\lambda)}{3ak\lambda^2} \right) \frac{9 + 3c^{-1}(\lambda^3 + 3\lambda^2 + 7\lambda) + \lambda^4c^{-2}}{3(3 + 2\lambda) + 2\lambda^2c^{-1}}, \quad (74)$$

from which the non-monotonicity in  $\lambda$  is more easily argued.

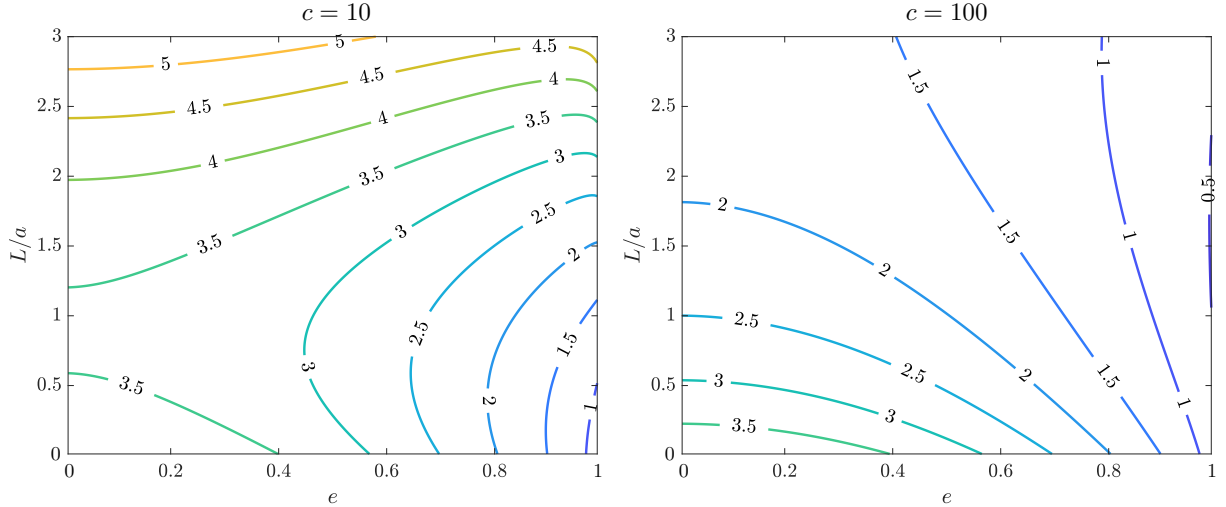


FIG. 2. Contours of the dimensionless function  $\mathcal{F}$  are shown, where  $e$  is the cell body eccentricity,  $\lambda = L/a$  is the relative flagellum length, and  $M_a^* = [Bc/(ak\lambda^2\ell_h)]\mathcal{F}$  is the critical active moment beyond which a straight swimming trajectory is unstable (to leading order in the flagellar amplitude). The critical active moment is generically non-monotonic in the flagellum length.

For a very slender flagellum  $c \gg 1$  (e.g. with  $c = 100$  in the right-most panel of Fig. 2), a longer flagellum tends to result in greater orientational instability since the moment applied at its base by the flagellar hook is fixed, but the viscous resistance to realigning the flagellum to the normal direction is increased. However, the stability of this configuration also depends on the flagellum slenderness, via the prefactor  $c/(ak\lambda^2)$  in  $\tilde{M}_a^*$ . As  $c \rightarrow \infty$  the normal orientation is stable, as the resistance to returning the filament to the normal direction is reduced. In practice, however,  $c$  is logarithmic in the filament slenderness, and  $c$  is more likely to be on the scale of  $10 - 100$  [2]. At leading order for large  $c$  we do not observe a dependence of stability on the flagellum amplitude, but we do observe a dependence on the flagellum wavenumber, owing to the discussion at the end of §IV(c). The hook is stabilized with a smaller wavenumber  $k$  or a longer flagellar wavelength (again by the prefactor above), since a given motor torque then generates a smaller thrust, all else being equal. Chirality is important, however: changing the sign of the active moment results in a reversal in the flagellum rotation direction, rendering the unstable regimes above stable; namely,  $\phi = 0$  is always a stable equilibrium in this model if the flagellum is pulling on the cell body. For a slender cell body,  $e \approx 1$ , we find  $\tilde{M}_a^* \sim 4ca/[kL^2((L_e - 1)\lambda + L_e)] + O(1)$  as  $e \rightarrow 1$ , with  $L_e = \log[(1 + e)/(1 - e)]$ , further highlighting the competition between the slenderness of the flagellum and the slenderness of the cell body.

To summarize, if the preferred flagellum orientation is normal to the cell surface, a straight swimming path is predicted for motor torques below a critical value. For motor torques beyond a critical value, which is generically non-monotonic in the flagellum length, the normal orientation is unstable, and the hook angle  $\phi$  must equilibrate at another value, as dictated by the autonomy of the dynamical system. In that configuration, the trajectory is assured to be helical, given the discussion in §II, a point to which we will shortly return.

## 2. Arbitrary preferred hook angle and helical trajectories

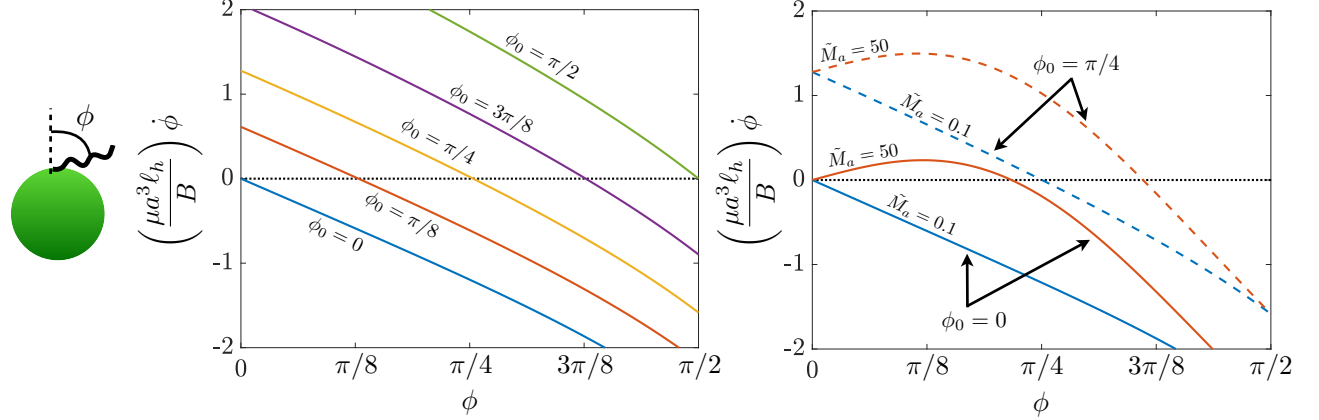


FIG. 3.  $e = 0$ . (Left) The dimensionless hook bending rate as a function of the current hook angle is shown for a selection of preferred hook angles,  $\phi_0$ , with dimensionless active motor torque,  $\tilde{M}_a = 1$ . The body is spherical,  $e = 0$ , and the remaining dimensionless parameters are  $c = 10$ ,  $kL = 1$ , and  $\lambda = L/a = 1$ . (Right) The same, but for two different values of the dimensionless active motor torque  $\tilde{M}_a$ , and two different preferred hook angles.

Finally we consider the case that the preferred flagellar orientation is not normal to the cell,  $\phi_0 \neq 0$ . Figure 3 (left) shows the dimensionless hook bending rate  $\dot{\phi}$  as a function of the current bending angle  $\phi$  for a selection of preferred angles  $\phi_0$ , with dimensionless active motor torque,  $\tilde{M}_a = M_a/(B/\ell_h) = 1$ . For these plots the body is assumed spherical,  $e = 0$ , and the remaining dimensionless parameters are chosen as follows:  $c = 10$ ,  $kL = 1$ , and  $\lambda = 1$ . An angle  $\phi^*$  which is slightly larger than  $\phi_0$  is observed to be stable. But upon increasing the motor torque,  $\dot{\phi}$  can become non-monotonic, as shown in Fig. 3 (right), which includes two preferred angles,  $\phi_0 = 0$  and  $\phi_0 = \pi/4$ , and two dimensionless motor torques  $\tilde{M}_a = 0.1$  and  $\tilde{M}_a = 50$ . The straight swimming case, studied in the previous section, reveals a pitchfork bifurcation beyond a critical  $\tilde{M}_a$  in between these values (or a supercritical Hopf bifurcation if viewed as a two-dimensional system describing the flagellum tip position). If  $\phi_0 > 0$ , however, the non-monotonicity of  $\dot{\phi}$  does not affect the stability of the fixed point, it merely nudges the fixed point closer to  $\pi/2$ .

Another view of the dynamics is provided by focusing on the path taken by the tip of the flagellum in the body frame. The top row of Fig. 4 shows the dynamics of the flagellar tip when  $\phi_0 = 0$  for an active moment substantially larger than the critical moment, one commensurate with but just below that critical value, and one which is much smaller than the critical value. The unstable case involves many rotations and a slow departure away from the normal direction, the commensurate case shows oscillations with exponential decay towards the equilibrium, and the final case reveals an overdamped decay to the preferred orientation. The second row of Fig. 4 shows the flagellum tip dynamics with a preferred hook angle of  $\phi_0 = \pi/4$ , showing similar dynamical structure as in the  $\phi_0 = 0$  case. When the active moment is small the hook angle rapidly adjusts to nearly the preferred angle,  $\phi_0$ , then the flagellum precesses around the normal direction with a constant rotation rate.

Once the dynamical system above has selected the fixed point,  $\phi^*$ , such that  $\dot{\phi} = 0$ , the body moves along a helical trajectory. Performing a simple numerical root-finding algorithm on Eq. (59) and evaluating  $\mathbf{U}_0$  and  $\mathbf{\Omega}_0$  at this angle, the helical amplitude  $\kappa/(\kappa^2 + \tau^2)$ , and the pitch angle  $\tan^{-1}(\kappa/|\tau|)$  are quickly computed using the expressions in §II. Figure 5 shows contours of the equilibrium bending angle, amplitude, and pitch angle as functions of the dimensionless motor torque  $\tilde{M}_a = M_a/(B/\ell_h)$  and the preferred hook angle  $\phi_0$ . To generate these plots we use biologically relevant material parameters, taking values describing an organism with a single polar flagellum, *P. aeruginosa*, from Refs. [62, 63], and assuming the ‘normal form’ of the flagellum. The cell body has half-length  $a = 1\mu\text{m}$  and aspect ratio 4, giving an eccentricity  $e = \sqrt{15}/4 \approx 0.97$ . The relative flagellum length is taken to be  $\lambda = L/a = 2$ , the helical radius is  $b = 0.2\mu\text{m}$  and the pitch is  $P = 1.4\mu\text{m}$ , so we take  $k = 2\pi/\sqrt{P^2 + 4\pi^2 b^2} = 3.34\mu\text{m}^{-1}$ .

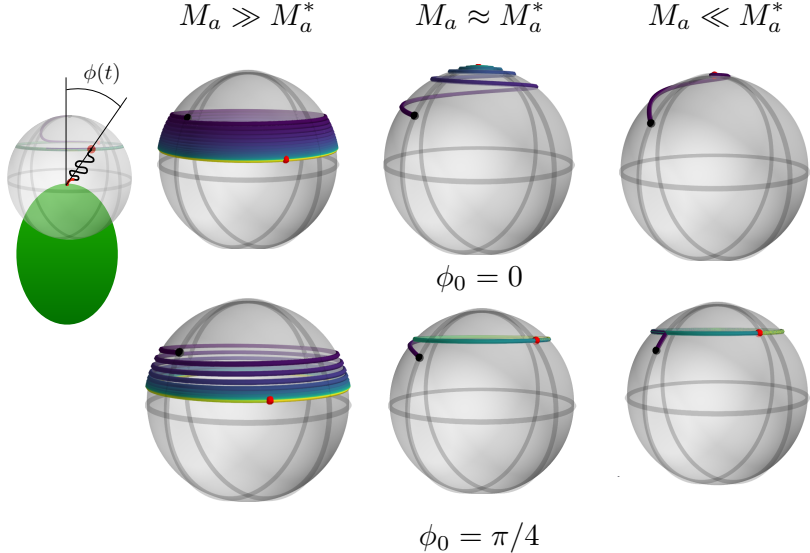


FIG. 4. The dynamics of the flagellar tip, represented as motion on a sphere (see schematic on the left). The preferred hook angle is  $\phi_0 = 0$  (top row) or  $\phi_0 = \pi/4$  (bottom row). Left column: large motor torque applied to the flagellum results in flagellum orientation instability and the tip slowly winds down towards a large equilibrium hook angle. Center column: with the motor torque very near to but below the critical motor torque for instability, the flagellum orientation relaxes to an equilibrium after a few precessions. Right column: for very small motor torques, the bending stiffness of the hook overwhelms any other effects and the orientation returns to the preferred angle exponentially fast in time. The dynamics of the tip are consistent with a supercritical Hopf bifurcation.

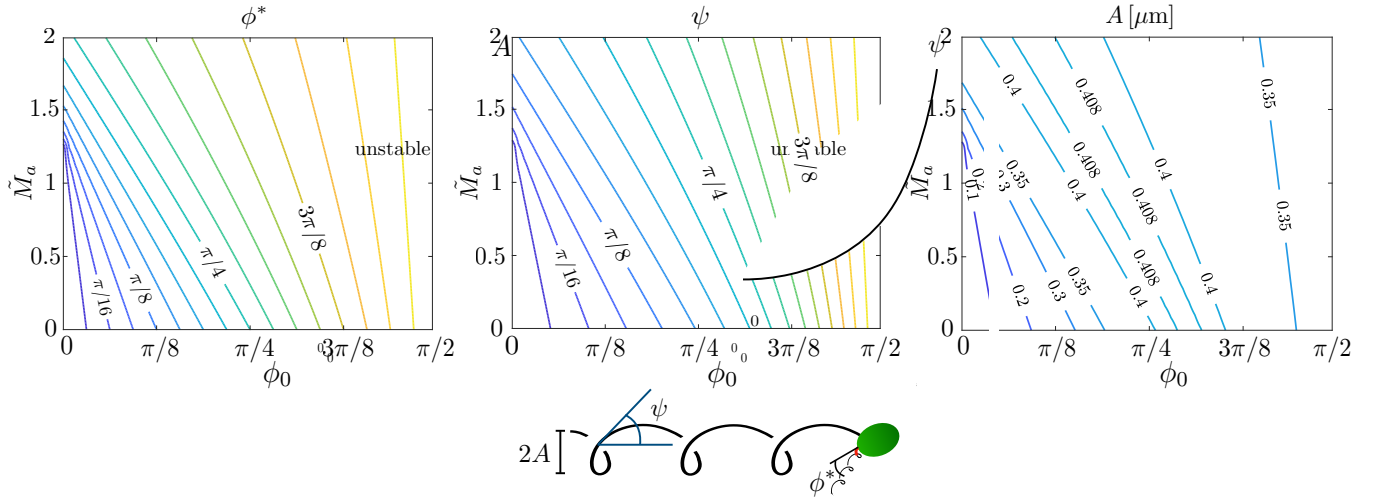


FIG. 5. Helical swimming trajectories using physical constants measured for *P. aeruginosa*. (Left) Equilibrium hook angle; (center) helical trajectory pitch angle; (right) helical trajectory amplitude. Across a wide range of hook angles the helical amplitudes remains in a very small range around a maximum near  $A \approx 0.4\mu\text{m}$

The flagellum aspect ratio is  $\varepsilon = 20\text{nm}/4\mu\text{m} = 0.005$ , which gives  $c = -\log(\varepsilon^2) - 1 \approx 10$ .

The equilibrium pitch angle is an increasing function of the motor torque and is only non-smooth (but still continuous, consistent with Ref. [41]) for  $\phi_0 = 0$ . Large motor torques nudge the equilibrium angle towards  $\pi/2$ , and the flagellum closer to the tangent plane of the cell body at the hook connection point. The helical pitch angle transitions from small (nearly straight swimming) for  $\phi_0 = 0$  and small motor torque to values closer to  $\pi/2$  (and a tightly coiled path) for similarly large preferred hook angles. The pitch angle of the helical trajectory tends to be smaller than the equilibrium hook bending angle, as it incorporates the full hydrodynamic coupling with the cell body. Finally, the

helical amplitude shows a remarkable feature. As soon as the equilibrium hook angle is not very small, either because the preferred angle is not small, or because the motor torque is large, the helical amplitude remains in a very small range around a maximum near  $A \approx 0.4\mu\text{m}$ . We might expect, then, to find *P. aeruginosa* cells swimming along a variety of helical paths with different pitch angles but very similar helical amplitudes.

## V. DISCUSSION

We have aimed to isolate the role of a flexible flagellar hook in microorganism locomotion by studying a model phase-averaged rigid helical flagellum. The mathematical simplicity offered by this modeling choice allowed for the analytical prediction of a critical stability criterion for the motor torque beyond which the flagellum hook angle becomes unstable, a prediction which included details about the flagellum geometry. This constraint also indicates that the straight- or nearly-straight swimming of some flagellated microorganisms might not be possible beyond a maximum speed, as increasing the motor torque to increase the thrust may destabilize the trajectory. This is reminiscent of a tradeoff made in vastly larger organisms like fish, which exploit flexible appendages for speed and efficiency benefits, but beyond a critical flapping frequency the appendage deformability can result in dramatically poor performance, even retrograde motion [64–66]. The constraints on the flagellar hook flexibility, and the functionality conferred by its deformability, may lead to deeper insights about the evolutionary development of flagellar cell motility. Observations of natural motility continues to motivate the creation of synthetic analogues [67–73], bio-hybrids [74], and even energy harvesting applications [75]. Many organisms swim through fluids which are substantially non-Newtonian, and the additional physical forces conferred on the helical flagellum (and the cell body) by shear-dependent viscosity [76, 77] and viscoelasticity [78–85], for instance, are likely to contribute to these buckling criteria as well, just as they can affect the dynamics of flagellar bundling [86].

Among our findings we have shown that straight-swimming is less stable for longer flagella or for cell bodies with a smaller aspect ratio, in the sense that the active motor torque required to destabilize straight swimming is decreased. On the other hand, when the flagellum is vanishingly thin, there is very little resistance to returning the flagellum to the preferred hook angle. The final outcome depends on all parameters, including the relative flagellum length and helical wavenumber, and the cell body eccentricity. But once the hook angle settles to its equilibrium, the cell body still traverses a helical path, even as the flagellum precesses and the cell body translates and rotates. The stability of the body trajectory is substantially softened when the preferred hook angle is non-zero, in the sense that the resulting helical trajectory appears to have a much smoother dependence on the active moment applied to the hook at the base of the flagellum. This raises the question of whether the non-zero spontaneous hook angle may have arisen in part to confer a more predictable path through the fluid, predictability upon which other biological functions might develop like flow-enhanced molecular transport [87], albeit along a dizzying helical trajectory.

## Appendix A: Cell translation and rotation rates

In the full problem of a freely swimming cell body, solving Eqs. (47)–(50) we find the body translation in the reference frame,

$$\begin{aligned} \mathbf{U}_0 = & \frac{-M_a}{12\pi\mu a L X^A} \left( \frac{X^A}{Y^A} m_2 \sin(2\phi) \mathbf{e}_1 + 3 \frac{X^A}{Y^A} m_3 \sin(\phi) \mathbf{e}_2 + (m_1 + m_2 \cos(2\phi)) \mathbf{e}_3 \right) \\ & + \frac{B}{6\pi\mu a L \ell_h X^A} \left\{ 3 \frac{X^A}{Y^A} m_3 \left( \sin(\phi) - \tan\left(\frac{\phi_0}{2}\right) \cos(\phi) - \tan\left(\frac{\phi}{2}\right) \right) \mathbf{e}_1 + (m_1 - m_2) \frac{X^A}{Y^A} \left( \tan\left(\frac{\phi}{2}\right) - \tan\left(\frac{\phi_0}{2}\right) \right) \mathbf{e}_2 \right. \\ & \quad \left. - 3m_3 \left( 1 - \cos(\phi) - \tan\left(\frac{\phi_0}{2}\right) \sin(\phi) \right) \mathbf{e}_3 \right\} + O(\lambda/c), \quad (A1) \end{aligned}$$

and the rotation rate,

$$\boldsymbol{\Omega}_0 = \frac{-M_a}{8\pi\mu a^3 X^C} \left( -\frac{3m_3 X^C}{2\lambda Y^C} \sin(\phi) \mathbf{e}_1 + \frac{m_2 X^C}{2\lambda Y^C} \sin(2\phi) \mathbf{e}_2 + \mathbf{e}_3 \right) + \frac{B}{8\pi\mu a^2 L \ell_h Y^C} \left( \tan\left(\frac{\phi}{2}\right) - \tan\left(\frac{\phi_0}{2}\right) \right) ((m_2 - m_1) \mathbf{e}_1 + (2\lambda + 3m_3 \cos(\phi)) \mathbf{e}_2) + O(\lambda/c), \quad (\text{A2})$$

as  $c/\lambda \rightarrow \infty$ , where we have defined the scaled flagellum length  $\lambda = L/a$  and  $m_1$ ,  $m_2$ , and  $m_3$  are given in § IV E. The component of the flagellum rotation rate relevant to the bending angle dynamics is

$$\mathbf{e}_2 \cdot \boldsymbol{\Omega}_0^f = \frac{M_a Q_1}{8\pi\mu a L^2} m_3 \sin(\phi) (m_1 + m_2 \cos(2\phi)) - \frac{B}{8\pi\mu \ell_h L^3} \left( 2c\eta + \frac{3\lambda^2 m_3}{Y^C} + 3\lambda m_3^2 (Q_2 + Q_1 \cos(2\phi)) \right) \left( \tan\left(\frac{\phi}{2}\right) - \tan\left(\frac{\phi_0}{2}\right) \right) + O(\lambda/c), \quad (\text{A3})$$

with

$$Q_1 = \frac{3}{4Y^C} + \frac{1}{Y^A} - \frac{1}{X^A}, \quad Q_2 = \frac{1}{X^A} + \left( 1 + 2 \left( \frac{\beta_2}{\beta_3} \right)^2 \right) \left( \frac{1}{Y^A} + \frac{3}{4Y^C} \right), \quad (\text{A4})$$

and  $\eta$  given in Eq. (52). Although  $c/\lambda = ca/L$  is assumed large for the expressions above, no such assumption is made when presenting the hook bending rate, Eq. (59) in the main text, and we find

$$C_1(\phi) = \frac{1}{3\alpha_1\alpha_2 X^A X^C Y^C (3\alpha_2 + c^{-1}\lambda Q_3) \nu(\phi)} (cM_1 + M_0 + c^{-1}M_{-1} + c^{-2}M_{-2} + c^{-3}M_{-3}), \quad (\text{A5})$$

$$C_2(\phi) = \frac{N_0 + c^{-1}N_{-1} + c^{-2}N_{-2}}{3(3\alpha_2 + c^{-1}\lambda Q_3) \nu(\phi)}, \quad (\text{A6})$$

where we have defined  $Q_3 = 3/Y^C + 4/Y^A$  and

$$\nu(\phi) = 1 + \frac{\lambda}{6c} \left( \left( \frac{1}{\alpha_2} + \frac{1}{\alpha_1} \right) \left( Q_3 + \frac{4}{X^A} \right) + 4 \left( \frac{1}{\alpha_2} - \frac{1}{\alpha_1} \right) Q_1 \cos(2\phi) \right) + \frac{4\lambda^2}{9c^2} \frac{Q_3}{\alpha_1\alpha_2 X^A}, \quad (\text{A7})$$

and the coefficients are as follows:  $M_1 = 18(\alpha_2\eta\nu(\phi) - \beta_3^2(1 - \nu(\phi)))$ ,

$$M_0 = 18\lambda^3 \alpha_1 \alpha_2^2 X^A Y^A - 36\lambda^2 \alpha_1 \alpha_2 \beta_3 X^A Y^A \cos(\phi) + 3\lambda Y^A Y^C [4\alpha_2 \beta_3^2 Q_1 X^A \cos(2\phi) - Q_3 X^A ((2\alpha_1 + \alpha_2)\beta_3^2 - 2\alpha_1\alpha_2\gamma_2\nu(\phi)) - 4\alpha_2\beta_3^2], \quad (\text{A8})$$

$$M_{-1} = 6\alpha_2\lambda^4 [\alpha_1 Q_3 X^A Y^A + 2(\alpha_1 + \alpha_2)(X^A + Y^A) + 2(\alpha_1 - \alpha_2)(X^A - Y^A) \cos(2\phi)] - 12\beta_3\lambda^3 Y^A (4\alpha_2 + \alpha_1 Q_3 X^A) \cos(\phi) - 4\lambda^2 \beta_3^2 Q_3 Y^A Y^C (2 + Q_1 X^A [1 - \cos(2\phi)]), \quad (\text{A9})$$

$$M_{-2} = 4\lambda^5 [8\alpha_2 + Q_3(\alpha_1 + \alpha_2)(X^A + Y^A) + Q_3(\alpha_1 - \alpha_2)(X^A - Y^A) \cos(2\phi)] - 16\lambda^4 \beta_3 Q_3 Y^A \cos(\phi), \quad (\text{A10})$$

and  $M_{-3} = 32\lambda^6 Q_3/3$ . Finally,

$$N_0 = \frac{9\lambda}{Y^C} \alpha_2 m_2 \cos(\phi) - 6\beta_3 Q_1 (m_1 + m_2 \cos(2\phi)), \quad (\text{A11})$$

$$N_{-1} = \frac{3m_2\lambda^2 Q_3 \cos(\phi)}{Y^C} + \frac{2\beta_3}{\alpha_1 \alpha_2} \lambda Q_3 Q_1 ((\beta_1 + \beta_2) + (\beta_1 - \beta_2) \cos(2\phi)) + \frac{12(\beta_2 - \beta_1)\lambda^2 \cos(\phi)}{\alpha_1 X^A Y^C}, \quad (\text{A12})$$

$$N_{-2} = \frac{4(\beta_2 - \beta_1)\lambda^3 Q_3 \cos(\phi)}{\alpha_1 \alpha_2 X^A Y^C}. \quad (\text{A13})$$

## ACKNOWLEDGEMENTS

We gratefully acknowledge helpful conversations with Michael Graham and Jean-Luc Thiffeault, and the support of the NSF/NIH (DMS-1661900) and the UW-Madison Welton Summer Sophomore Apprenticeship program.

---

[1] J. Lighthill. Flagellar hydrodynamics - JV Neumann lecture, 1975. *SIAM Review*, 18(2):161–230, 1976.

[2] C Brennen and H Winet. Fluid-mechanics of propulsion by cilia and flagella. *Ann. Rev. Fluid Mech.*, 9:339–398, 1977.

[3] R. M. Macnab. Bacterial flagella rotating in bundles: a study in helical geometry. *Proc. Natl. Acad. Sci.*, 74(1):221–225, 1977.

[4] F. A. Samatey, H. Matsunami, K. Imada, S. Nagashima, T. R. Shaikh, D. R. Thomas, J. Z. Chen, D. J. DeRosier, A. Kitao, and K. Namba. Structure of the bacterial flagellar hook and implication for the molecular universal joint mechanism. *Nature*, 431(7012):1062, 2004.

[5] S. M. Block, D. F. Blair, and H. C. Berg. Compliance of bacterial flagella measured with optical tweezers. *Nature*, 338:514–518, 1989.

[6] S. M. Block, D. F. Blair, and H. C. Berg. Compliance of bacterial polyhooks measured with optical tweezers. *Cytometry*, 12:492–496, 1991.

[7] A. Sen, R. K. Nandy, and A. N. Ghosh. Elasticity of flagellar hooks. *Microscopy*, 53(3):305–309, 2004.

[8] T. C. Flynn and J. Ma. Theoretical analysis of twist/bend ratio and mechanical moduli of bacterial flagellar hook and filament. *Biophys. J.*, 86:3204–3210, 2004.

[9] T. Pilizota, M. T. Brown, M. C. Leake, R. W. Branch, R. M. Berry, and J. P. Armitage. A molecular brake, not a clutch, stops the Rhodobacter sphaeroides flagellar motor. *Proc. Natl. Acad. Sci. USA*, 106(28):11582–11587, 2009.

[10] K. Son, J. S. Guasto, and R. Stocker. Bacteria can exploit a flagellar buckling instability to change direction. *Nature Phys.*, 9:494–498, 2013.

[11] M. T. Brown, B. C. Steel, C. Silvestrin, D. A. Wilkinson, N. J. Delalez, C. N. Lumb, B. Obara, J. P. Armitage, and R. M. Berry. Flagellar hook flexibility is essential for bundle formation in swimming Escherichia coli cells. *J. Bacteriol.*, 194:3495–3501, 2012.

[12] I. Spöring, V. A. Martinez, C. Hotz, J. Schwarz-Linek, K. L. Grady, J. M. Nava-Sedeño, T. Vissers, H. M. Singer, M. Rohde, C. Bourquin, et al. Hook length of the bacterial flagellum is optimized for maximal stability of the flagellar bundle. *PLoS Biol.*, 16(9), 2018.

[13] L. Xie, T. Altindal, S. Chattopadhyay, and X.-L. Wu. Bacterial flagellum as a propeller and as a rudder for efficient chemotaxis. *Proc. Natl. Acad. Sci.*, 108(6):2246–2251, 2011.

[14] N. C. Darnton, L. Turner, S. Rojevsky, and H. C. Berg. On torque and tumbling in swimming Escherichia coli. *J. Bacteriol.*, 189:1756–1764, 2007.

[15] M. Jabbarzadeh and H. C. Fu. Dynamic instability in the hook-flagellum system that triggers bacterial flicks. *Phys. Rev. E*, 97:012402, 2018.

[16] M. Jabbarzadeh and H. C. Fu. Large deformations of the hook affect free-swimming singly flagellated bacteria during flick motility. *Phys. Rev. E*, 102(3):033115, 2020.

[17] M. Palusa, J. De Graaf, A. Brown, and A. Morozov. Sedimentation of a rigid helix in viscous media. *Phys. Rev. Fluids*, 3:124301, 2018.

[18] H. O. Caldag and S. Yesilyurt. Trajectories of magnetically-actuated helical swimmers in cylindrical channels at low Reynolds numbers. *J. Fluids and Struct.*, 90:164–176, 2019.

[19] K. Samsami, S. A. Mirbagheri, F. Meshkati, and H. C. Fu. Stability of soft magnetic helical microrobots. *Fluids*, 5(1):19, 2020.

[20] D. Das and E. Lauga. Transition to bound states for bacteria swimming near surfaces. *Phys. Rev. E*, 100(4):043117, 2019.

[21] K. Ishimoto. Bacterial spinning top. *J. Fluid Mech.*, 880:620–652, 2019.

[22] K. Ishimoto. Helicoidal particles and swimmers in a flow at low Reynolds number. *J. Fluid Mech.*, 892, 2020.

[23] J. Zhang, M. Chinappi, and L. Biferale. Base flow decomposition for complex moving objects in linear hydrodynamics: Application to helix-shaped flagellated microswimmers. *Phys. Rev. E*, 103:023109, 2021.

[24] S. Jung, K. Mareck, L. Fauci, and M. J. Shelley. Rotational dynamics of a superhelix towed in a Stokes fluid. *Phys. Fluids*, 19(10), 2007.

[25] O. S. Pak, S. E. Spagnolie, and E. Lauga. Hydrodynamics of the double-wave structure of insect spermatozoa flagella. *J. Roy. Soc. Interface*, 9:1908–1924, 2012.

[26] J. T Pham, A. Morozov, A. J. Crosby, A. Lindner, and O. du Roure. Deformation and shape of flexible, microscale helices in viscous flow. *Phys. Rev. E*, 92:011004, 2015.

[27] M. K. Jawed, N. K. Khouri, F. Da, E. Grinspan, and P. M. Reis. Propulsion and instability of a flexible helical rod rotating in a viscous fluid. *Phys. Rev. Lett.*, 115:168101, 2015.

[28] B. Chakrabarti, Y. Liu, J. LaGrone, R. Cortez, L. Fauci, O. du Roure, D. Saintillan, and A. Lindner. Flexible filaments buckle into helicoidal shapes in strong compressional flows. *Nature Phys.*, 16:689–694, 2020.

[29] H. S. Jennings. On the significance of the spiral swimming of organisms. *The American Naturalist*, 35(413):369–378, 1901.

[30] H. C. Crenshaw. Orientation by helical motion I. Kinematics of the helical motion of organisms with up to six degrees of freedom. *Bull. Math. Biol.*, 55(1):197–212, 1993.

[31] B. Liu, M. Gulino, M. Morse, J. X. Tang, T. R. Powers, and K. S. Breuer. Helical motion of the cell body enhances *Caulobacter crescentus* motility. *Proc. Natl. Acad. Sci.*, 111(31):11252–11256, 2014.

[32] Y. Hyon, T. R. Powers, R. Stocker, and H. C. Fu. The wiggling trajectories of bacteria. *J. Fluid Mech.*, 705:58–76, 2012.

[33] H. Shum and E. A. Gaffney. The effects of flagellar hook compliance on motility of monotrichous bacteria: A modeling study. *Phys. Fluids*, 24:061901, 2012.

[34] M. A. Constantino, M. Jabbarzadeh, H. C. Fu, Z. Shen, J. G. Fox, F. Haesebrouck, S. K. Linden, and R. Bansil. Bipolar lophotrichous *Helicobacter suis* combine extended and wrapped flagella bundles to exhibit multiple modes of motility. *Sci. Rep.*, 8(1):1–15, 2018.

[35] M. Rossi, G. Cicconofri, A. Beran, G. Noselli, and A. DeSimone. Kinematics of flagellar swimming in euglena gracilis: Helical trajectories and flagellar shapes. *Proc. Natl. Acad. Sci.*, 114(50):13085–13090, 2017.

[36] N. Giuliani, M. Rossi, G. Noselli, and A. DeSimone. How euglena gracilis swims: flow field reconstruction and analysis. *Phys. Rev. E*, 103(2):023102, 2021.

[37] A. Thawani and M. S. Tirumkudulu. Trajectory of a model bacterium. *J. Fluid Mech.*, 835:252, 2018.

[38] O. A. Croze, V. A. Martinez, T. Jakuszeit, D. Dell’Arciprete, W. C. K. Poon, and M. A. Bees. Helical and oscillatory microswimmer motility statistics from differential dynamic microscopy. *New J. Phys.*, 21:063012, 2019.

[39] D. Cortese and K. Y. Wan. Control of helical navigation by three-dimensional flagellar beating. *Phys. Rev. Lett.*, 126(8):088003, 2021.

[40] R. Vogel and H. Stark. Motor-driven bacterial flagella and buckling instabilities. *Euro. Phys. J. E*, 35(2):15, 2012.

[41] F. T. M. Nguyen and M. D. Graham. Buckling instabilities and complex trajectories in a simple model of uniflagellar bacteria. *Biophys. J.*, 112(5):1010–1022, 2017.

[42] F. T. M. Nguyen and M. D. Graham. Impacts of multiflagellarity on stability and speed of bacterial locomotion. *Phys. Rev. E*, 98(4):042419, 2018.

[43] J. Happel and H. Brenner. *Low Reynolds Number Hydrodynamics*. Prentice Hall, Inc., Englewood Cliffs, N.J., 1965.

[44] S. Childress. *Mechanics of Swimming and Flying*. Cambridge University Press, Cambridge U.K., 1981.

[45] J. D. Meiss. *Differential dynamical systems*. SIAM, 2007.

[46] S. Kim and S.J. Karrila. *Microhydrodynamics: Principles and Selected Applications*. Dover Publications, Inc., Mineola, NY, 1991.

[47] J. Gray and G. J. Hancock. The propulsion of sea-urchin spermatozoa. *J. Exp. Biol.*, 32(4):802–814, 1955.

[48] R. E. Johnson and C. J. Brokaw. Flagellar hydrodynamics—Comparison between resistive-force theory and slender-body theory. *Biophys. J.*, 25:113–127, 1979.

[49] K. Ishimoto and E. Lauga. The N-flagella problem: elastohydrodynamic motility transition of multi-flagellated bacteria. *Proc. Roy. Soc. A*, 475:20180690, 2019.

[50] B. Rodenborn, C.-H. Chen, H. L. Swinney, B. Liu, and H. P. Zhang. Propulsion of microorganisms by a helical flagellum. *Proc. Natl. Acad. Sci.*, 110(5), 2013.

[51] L. Li and S. E. Spagnolie. Swimming and pumping of rigid helical bodies in viscous fluids. *Phys. Fluids*, 26:041901, 2014.

[52] M. Bergou, M. Wardetzky, S. Robinson, B. Audoly, and E. Grinspun. Discrete elastic rods. In *ACM SIGGRAPH*, pages 1–12. 2008.

[53] O. M. O'Reilly. *Modeling Nonlinear Problems in the Mechanics of Strings and Rods*. Springer, 2017.

[54] D. G. Morgan, R. M. Macnab, N. R. Francis, and D. J. DeRosier. Domain organization of the subunit of the *Salmonella typhimurium* flagellar hook. *J. Mol. Biol.*, 229(1):79–84, 1993.

[55] T. Hirano, S. Yamaguchi, K. Oosawa, and S.-I. Aizawa. Roles of FliK and FlhB in determination of flagellar hook length in *Salmonella typhimurium*. *J. Bacteriol.*, 176:5439–5449, 1994.

[56] K. Kobayashi, T. Saitoh, D. S. H. Shah, K. Ohnishi, I. G. Goodfellow, R. E. Sockett, and S.-I. Aizawa. Purification and characterization of the flagellar basal body of *Rhodobacter sphaeroides*. *J. Bacteriol.*, 185:5295–5300, 2003.

[57] M. Koike, H. Terashima, S. Kojima, and M. Homma. Isolation of basal bodies with C-ring components from the Na<sup>+</sup>-driven flagellar motor of *Vibrio alginolyticus*. *J. Bacteriol.*, 192(1):375–378, 2010.

[58] M. Jabbarzadeh and H. C. Fu. A numerical method for inextensible elastic filaments in viscous fluids. *J. Comput. Phys.*, page 109643, 2020.

[59] L. Li, H. Manikantan, D. Saintillan, and S. E. Spagnolie. The sedimentation of flexible filaments. *J. Fluid Mech.*, 735:705–736, 2013.

[60] Y. Man and E. Kanso. Morphological transitions of axially-driven microfilaments. *Soft Matter*, 15(25):5163–5173, 2019.

[61] O. Du Roure, A. Lindner, E. N. Nazockdast, and M. J. Shelley. Dynamics of flexible fibers in viscous flows and fluids. *Annu. Rev. of Fluid Mech.*, 51:539–572, 2019.

[62] M. Fujii, S. Shibata, and S.-I. Aizawa. Polar, peritrichous, and lateral flagella belong to three distinguishable flagellar families. *J. Mol. Biol.*, 379:273–283, 2008.

[63] S. M. Vater, S. Weiße, S. Maleschlijski, C. Lotz, F. Koschitzki, T. Schwartz, U. Obst, and A. Rosenhahn. Swimming behavior of *Pseudomonas aeruginosa* studied by holographic 3d tracking. *PLoS one*, 9:e87765, 2014.

[64] J. H. Long Jr. and K. S. Nipper. The importance of body stiffness in undulatory propulsion. *Am. Zool.*, 36(6):678–694, 1996.

[65] S. Alben, P. G. Madden, and G. V. Lauder. The mechanics of active fin-shape control in ray-finned fishes. *J. Roy. Soc. Inter.*, 4(13):243–256, 2007.

[66] S. E. Spagnolie, L. Moret, M. J. Shelley, and J. Zhang. Surprising behaviors in flapping locomotion with passive pitching. *Phys. Fluids*, 22(4):041903, 2010.

[67] S. J. Ebbens and J. R. Howse. In pursuit of propulsion at the nanoscale. *Soft Matter*, 6:726–738, 2010.

[68] B. J. Nelson, I. K. Kaliakatsos, and J. J. Abbott. Microrobots for minimally invasive medicine. *Annu. Rev. Biomed. Eng.*, 12(1):55–85, 2010.

[69] S. Sengupta, M. E. Ibele, and A. Sen. Fantastic voyage: Designing self-powered nanorobots. *Angew. Chem. Int. Ed.*, 51(34):8434–8445, 2012.

[70] J. Li, B. Esteban-Fernández de Ávila, W. Gao, L. Zhang, and J. Wang. Micro/nanorobots for biomedicine: Delivery, surgery, sensing, and detoxification. *Sci. Robot.*, 2(4), 2017.

[71] L. Ricotti, B. Trimmer, A. W. Feinberg, R. Raman, K. K. Parker, R. Bashir, M. Sitti, S. Martel, P. Dario, and A. Menciassi. Biohybrid actuators for robotics: A review of devices actuated by living cells. *Sci. Robot.*, 2(12), 2017.

[72] C. Hu, S. Pane, and B. J. Nelson. Soft micro- and nanorobotics. *Annual Review of Control, Robotics, and Autonomous Systems*, 1(1):53–75, 2018.

[73] A. C. H. Tsang, E. Demir, Y. Ding, and O. S. Pak. Roads to smart artificial microswimmers. *Adv. Intell. Syst. Comput.*, 2(8):1900137, 2020.

[74] R. W. Carlsen and M. Sitti. Bio-hybrid cell-based actuators for microsystems. *Small*, 10(19):3831–3851, 2014.

[75] L. Zhu and H. A. Stone. Harnessing elasticity to generate self-oscillation via an electrohydrodynamic instability. *J. Fluid Mech.*, 888, 2020.

[76] S. Gómez, F. A. Godínez, E. Lauga, and R. Zenit. Helical propulsion in shear-thinning fluids. *J. Fluid Mech.*, 812, 2017.

[77] E. Demir, N. Lordi, Y. Ding, and O. S. Pak. Nonlocal shear-thinning effects substantially enhance helical propulsion. *Phys. Rev. Fluids*, 5(11):111301, 2020.

[78] H. C. Fu, T. R. Powers, and H. C. Wolgemuth. Theory of swimming filaments in viscoelastic media. *Phys. Rev. Lett.*, 99:258101–258105, 2007.

- [79] H. C. Fu, C. W. Wolgemuth, and T. R. Powers. Swimming speeds of filaments in nonlinearly viscoelastic fluids. *Phys. Fluids*, 21:033102, 2009.
- [80] L. Li and S. E. Spagnolie. Swimming and pumping by helical waves in viscous and viscoelastic fluids. *Phys. Fluids*, 27:021902, 2015.
- [81] B. Liu, T. R. Powers, and K. S. Breuer. Force-free swimming of a model helical flagellum in viscoelastic fluids. *Proc. Natl. Acad. Sci.*, 108:19516–19520, 2011.
- [82] S. E. Spagnolie, B. Liu, and T. R. Powers. Locomotion of helical bodies in viscoelastic fluids: enhanced swimming at large helical amplitudes. *Phys. Rev. Lett.*, 111:068101, 2013.
- [83] V. A. Martinez, J. Schwarz-Linek, M. Reufer, L. G. Wilson, A. N. Morozov, and W. C. K. Poon. Flagellated bacterial motility in polymer solutions. *Proc. Natl. Acad. Sci.*, 111:17771–17776, 2014.
- [84] A. Zöttl and J. M. Yeomans. Enhanced bacterial swimming speeds in macromolecular polymer solutions. *Nature Phys.*, 15:554–558, 2019.
- [85] J. P. Binagia, A. Phoa, K. D. Housiadas, and E. S. G. Shaqfeh. Swimming with swirl in a viscoelastic fluid. *J. Fluid Mech.*, 900, 2020.
- [86] Z. Qu and K. S. Breuer. Effects of shear thinning viscosity and viscoelastic stresses on flagellated bacteria motility. *Phys. Rev. Fluids*, 5(11):073103, 2020.
- [87] M. B. Short, C. A. Solari, S. Ganguly, T. R. Powers, J. O. Kessler, and R. E. Goldstein. Flows driven by flagella of multicellular organisms enhance long-range molecular transport. *Proc. Natl. Acad. Sci. USA*, 103:8315–8319, 2006.